# First-principles study of charge-transfer-plasmon-enhanced photoemission from a gold-nanoparticle–sodium-atom emitter

Zhexuan Wang, Fang Liu,[*] Kaiyu Cui, Xue Feng, Wei Zhang, and Yidong Huang[†]

*Department of Electronic Engineering, Tsinghua University, Beijing 100084, China*
*and Beijing National Research Center for Information Science and Technology, Tsinghua University, Beijing 100084, China*

The plasmon-enhanced photoemission process significantly improves the quality of electron emission current, making it applicable for next-generation free-electron devices. However, classical descriptions are less suitable for understanding the interactions between plasmonic structures and other materials at the nanoscale. In this study, we investigate the underlying mechanisms and dynamics of a plasmonic emitter composed of a Au nanoparticle and a sodium atom using real-time time-dependent density functional theory. Calculation results reveal three interaction mechanisms, namely, a near-field enhancement effect, orbital hybridization, and charge-transfer plasmon, that strongly affect the emission behavior. Specifically, the presence of the charge-transfer plasmon leads to a substantial deviation of the excitation laser frequency and significantly enhances photoemission currents. The maximum emission current increases by more than twice compared to the excitation at the original resonance frequency of Au nanoparticles. This work provides a guidance for the practical construction and experimentation of plasmon-enhanced photoemission electron sources.

## I. INTRODUCTION

Plasmonic structures have played a crucial role in enhancing the light-matter interaction, including enhancing the light absorption of active materials [1–4] and increasing the electron emission current of free-electron devices [5–13]. According to classical descriptions, the enhancement of photoemission by plasmons is primarily due to the near-field enhancement (NFE), where the intensified interactions with light lead to enhanced excitations in the emitters, helping them absorb more photons. It is believed that the maximum enhancement of photoemission current is achieved when the input laser frequency is exactly at the plasmonic resonance frequency. However, classical theory describing structures with clear boundaries and without considering underlying quantum effects is less appropriate for understanding the interactions between plasmonic materials and other materials at the nanoscale [14,15], which is often relevant for junctionlike heterogeneous electron sources involving metallic nanostructures with two-dimensional materials or thin-film emitters [16,17].

In nanoscale plasmonic metal clusters, an important form of excitation is known as localized surface plasmon resonance (LSPR), which is composed of collective oscillations of electron density with external electromagnetic fields [18]. When plasmonic structures are close to target materials or structures, new interaction mechanisms would emerge, such as orbital hybridization (OH) and charge transfer plasmons (CTPs) [19,20]. Among them, the CTP involves collective charge transfers between electronic states of two objects, significantly modifying the optical and electrical response

properties of the system. For example, in closely connected dimers or those with sufficient electron cloud overlap, CTP peaks appear at the lower-energy region of the absorption spectrum compared to that without electron cloud overlap [20]. Others found that the CTP drastically reduced the electromagnetic field enhancement at interparticle distance below 1 nm, compared to classical predictions [21,22]. Also, recent research showed that the coupling between a dimer and an intermediate metallic nanoparticle also changed the optical resonance characteristics and light radiation of the system [23]. Obviously, there is every reason that the photoemission process from a nanoscale plasmonic emitter exhibits unexpected behaviors and the optimal incident laser frequency deviates from classical predictions. Hence, further research is needed to explore the new phenomena arising from these mechanisms, especially investigating CTPs in the plasmonic-enhanced photoemission process at the nanoscale.

In this study, we investigate the electron emission from a plasmonic emitter composed of an Au nanoparticle (NP) and a sodium (Na) atom. Analysis of the underlying quantum mechanisms is performed by real-time time-dependent density functional theory (TDDFT). The results reveal that the optimal laser frequency for exciting the plasmonic emitter gradually deviates away from the original plasmonic resonance frequency of the NP as the distance between the Au NP and the Na atom decreases. This is because the effect of the CTP at different frequency gradually replaces the classical NFE for the photoemission current in a close distance. The maximum emission current is increased by more than twice compared to that excited by the original Au-NP plasmonic resonant frequency. Additionally, we find that NFE, OH, and the CTP sequentially influence the emission process as the Au NP and Na atom approach each other. The corresponding resonant modes and relative enhancement mechanisms are

---

[*]Corresponding author: liu_fang@mail.tsinghua.edu.cn
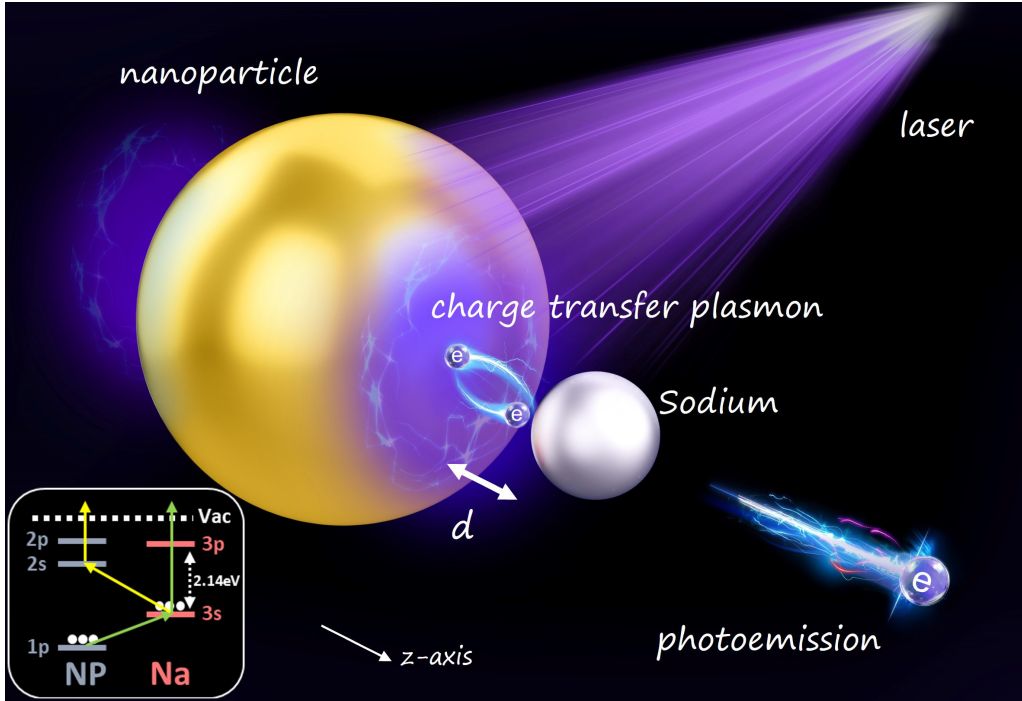[†]Corresponding author: yidonghuang@tsinghua.edu.cn

FIG. 1. The schematic of an electron emitter consisting of an Au nanoparticle and a sodium atom. A Gaussian laser beam is used for the emitter excitation with the light polarization direction aligned to the $z$ axis. The charge transfer plasmon (CTP) significantly affects the optimal laser excitation frequency and the enhancement of photoemission when distance $d$ is small.

revealed through calculations of absorption spectra, wave-function projections, and energy spectra. This work provides the guidance for the practical construction and experimentation of plasmon-enhanced photoemission electron sources.

## II. THEORETICAL MODELS AND NUMERICAL METHODS

### A. Theoretical models of NP-Na emitter

Figure 1 illustrates a closely spaced plasmonic emitter consisting of an Au NP and a Na atom. A Gaussian laser beam with polarization direction aligned to the $z$ axis induced photoemission from the emitter. A jellium model was utilized to describe the Au NP. Since the diameter of the Au NP has minimal impact on understanding the plasmonic interaction mechanisms [24,25], a cluster consisting of eight gold atoms is considered and only the $6s$ orbital electrons of each gold atom are regarded as valence electrons, so that the total electron number $N_e$ in jellium is set to eight, regarding the computational cost. The Wigner-Seitz radius of the Au species is $r_s = 1.6$ Å; hence the radius is $R = N_e^{1/3} r_s = 3.2$ Å. Modeling of the Na atom uses a local density approximation (LDA) and Troullier-Martins pseudopotentials. The distance $d$ between the Au NP and the Na atom varies from 9.6 to 0.8 Å. Within this range, the transition from NFE to CTP occurs, as discussed later. In the following text, the Au NP and Na atom are represented by NP and Na for short, respectively.

### B. TDDFT calculations

A fully quantum-mechanical description is essential to accurately describe the emission process of the closely spaced plasmonic emitters. Unlike the time-dependent Schrödinger equation (TDSE) [26–28], TDDFT [29–31] can handle many-body system problems in three dimensions and is considered an accurate reformulation of time-dependent quantum mechanics. In TDDFT, the time-dependent Kohn-Sham equation can be expressed as [30]

$$i\frac{\partial}{\partial t}\varphi_i(r, t) = H_{\text{KS}}(\rho)\,\varphi_i(r, t), \tag{1}$$

where $\varphi_i(r, t)$ are electron Kohn-Sham orbital wave functions. The Kohn-Sham Hamiltonian $H_{\text{KS}}(\rho)$ can be separated into several parts as follows:

$$H_{\text{KS}} = -\frac{1}{2}\nabla^2 + v_{\text{ext}}(r, t) + v_{\text{Hartree}}[n](r, t) + v_{\text{xc}}[n](r, t), \tag{2}$$

$$n(r, t) = \sum_i^{\text{occ}} |\varphi_i(r, t)|^2, \tag{3}$$

where $v_{\text{ext}}(r, t)$ represents the external field potential, $v_{\text{Hartree}}[n](r, t)$ is Hartree potential known as the classical electrostatic potential, and $v_{\text{xc}}[n](r, t)$ is exchange-correlation potential.

By solving the Kohn-Sham equation, the wave functions of electrons as a function of time and space are obtained. Then the current of photoemission is calculated according to the probability flow density formula [32–36]

$$j(r, t) = -\frac{i\hbar}{2}\sum\{\varphi_i^*(r, t)\nabla\varphi_i(r, t) - \varphi_i(r, t)\nabla\varphi_i^*(r, t)\}. \tag{4}$$
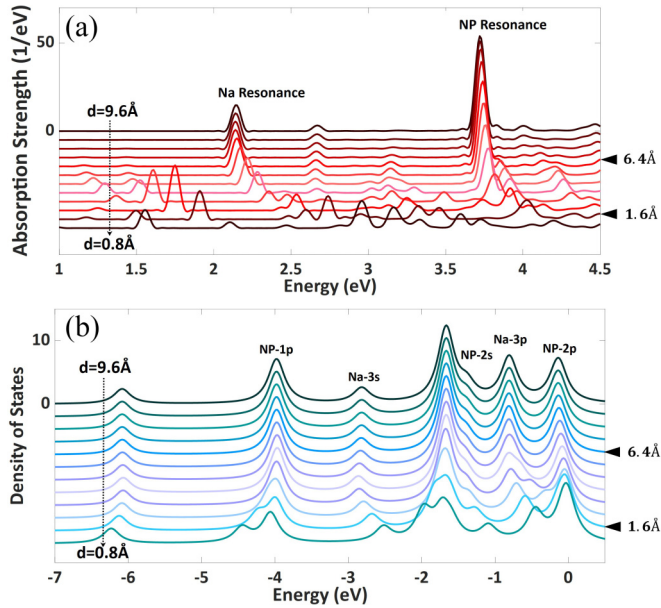
FIG. 2. (a) Absorption spectrum of the plasmonic emitter with varying $d$. Each peak in the spectrum corresponds to a resonance mode of the plasmonic emitter. (b) The density of states (DOS) of the plasmonic emitter with varying $d$. Each peak in the curve represents an electronic state and the peak magnitude represents the available state number.

To induce the photoemission, the Gaussian laser pulse

$$\boldsymbol{E}(t) = \hat{z} F \cos(\omega t) \exp\left[-\frac{(t-t_0)^2}{2\tau^2}\right] \qquad (5)$$

with pulse width $\tau = 2$ fs, $t_0 = 8$ fs, and $z$-polarized electric field is introduced. The calculation performs 20 000 steps with a time step of 0.003 fs.

### III. RESULTS AND DISCUSSIONS

#### A. Absorption spectrum and density of states

First, in order to observe how the incident laser interacts with the plasmonic emitter and gain a deeper understanding of the interaction mechanisms, the absorption spectrum and density of states (DOS) as a function of the distance $d$ are calculated, as shown in Fig. 2.

In Fig. 2(a), each peak in the absorption spectrum corresponds to a resonant mode of the plasmonic emitter. At larger $d$, the spectrum exhibits two sharp peaks at frequencies of 2.14 and 3.72 eV. The peak of 3.72 eV represents the LSPR of the NP, and the peak of 2.14 eV corresponds to the electron transition between the highest occupied molecular orbital (HOMO) andthe lowest unoccupied molecular orbital (LUMO) of Na, namely, Na 3$s$ to Na 3$p$. As $d$ decreases from 9.6 to 0.8 Å, there is an evident blueshift in both Na and NP resonant peaks, and the magnitude of the peaks weakens. Furthermore, when $d < 4$ Å, several additional peaks appear around 1.5 and 3 eV, which are attributed to the CTP. In addition, the original resonant mode peaks nearly vanish. The changes in the absorption spectrum are the consequences of the significant modification and disturbance of the original

resonant modes of both NP and Na due to their hybridizations of the electronic states and charge transfer interactions.

Figure 2(b) illustrates the DOS of the plasmonic emitter and each peak in the curve indicates electronic states and the available state number. We can also identify the electron orbitals by the projected density of states (PDOS), as shown in Fig. 2(b). The peaks in the DOS are consistent with the energy levels of the independent NP and Na. This indicates that the interaction between the two structures involves only NFE in this situation as the classical theory prediction. As $d$ decreases, the energy of Na orbitals undergoes a significant upward shift, while the energy of NP orbitals experiences a slight drop. When $d < 1.6$ Å, the DOS peak broadens and multiple branches emerge. Such phenomena are considered the strong interactions of OH and CTP between NP and Na, which has a significant impact on the electron transfer process and resonant frequency [37,38].

The calculation results of the absorption spectrum and DOS indicate that, at relatively large $d$, the interaction between NP and Na is dominated by classical NFE. There is no significant coupling or interference in their electron orbitals and resonant modes. As $d$ decreases to less than 6.4 Å, OH and the CTP would result in significant changes in the energy levels and plasmonic resonant modes. Not surprisingly, these interaction mechanisms would impact the photoemission behavior of a plasmonic emitter, which is indicated in view of the following qualitative analysis about the photoemission enhancement.

#### B. Analysis of photoemission current

Figure 3(a) depicts the photoemission current as a function of $d$. The blue solid curve with square markers, $I_0$, is derived under the illumination of the original plasmonic resonant frequency $f_0$ of the isolated NP, which was considered the optimal excitation frequency in classical theory. However, in Fig. 2(a), the frequency of the absorption peak varies with $d$, and it is natural to vary the excitation frequency to find the actual maximum photoemission current $I_{\max}$, which is depicted as the red dashed curve with circular markers, and the corresponding frequency is referred as $f_{\max}$. Figure 3(b) illustrates the $f_0$ with fixed value and the variation of $f_{\max}$, using the same marking style as those of Fig. 3(a). The $f_{\max}$ increases slightly as emitters gradually approach. A sudden decline of $f_{\max}$ occurs at 1.6 Å due to the CTP.

It can be seen from Fig. 3(a), when $d > 4.8$ Å, the red curve $I_{\max}$ is nearly consistent with the blue one, $I_0$, indicating that the laser frequency $f_0$ provides the maximum enhancement for large distance. Moreover, there is a clear increase in the emission current as the NP moves toward Na, demonstrating that the NFE from the NP primarily enhances the emission process of Na. This is consistent with the classical theory. In the plasmonic emitter, the presence of the NP enhances the local light field near Na, which increases the emission process by assisting in the light absorption. The NFE from the NP becomes very influential since the distance between them is smaller. Consequently, the emission current increases as the NP moves toward Na.

When $4 > d > 2.4$ Å, both $I_{\max}$ and $I_0$ exhibit a noticeable decrease. This is attributed to the involvement of the CTP and
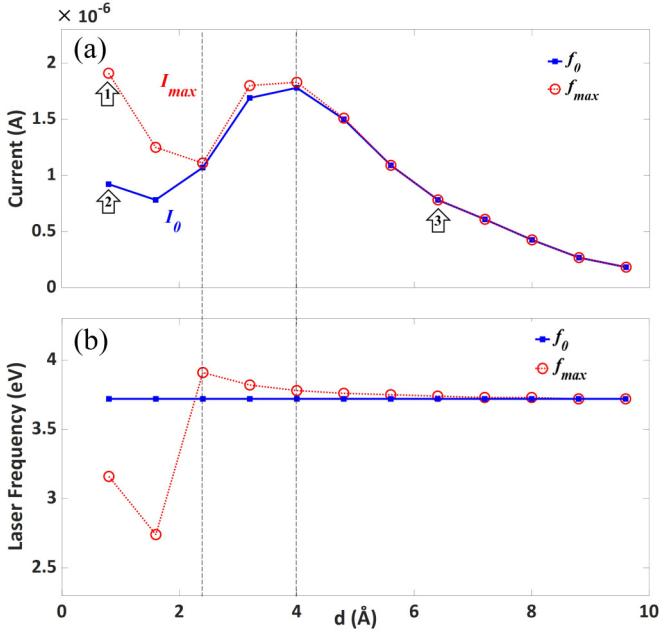
FIG. 3. (a) The photoemission current as a function of the distance $d$ between NP and Na. The blue solid curve with square markers, $I_0$, represents the photoemission current when the emitter is excited at the original plasmon resonance frequency of the NP. The red dashed curve with circular markers, $I_{max}$, represents the maximum photoemission current by varying the excitation frequency. (b) The corresponding incident laser frequency $f_0$ and $f_{max}$ of exciting the photoemission current in (a). The $f_{max}$ increases slowly at first, and decreases suddenly at 1.6 Å due to the involvement of the CTP.
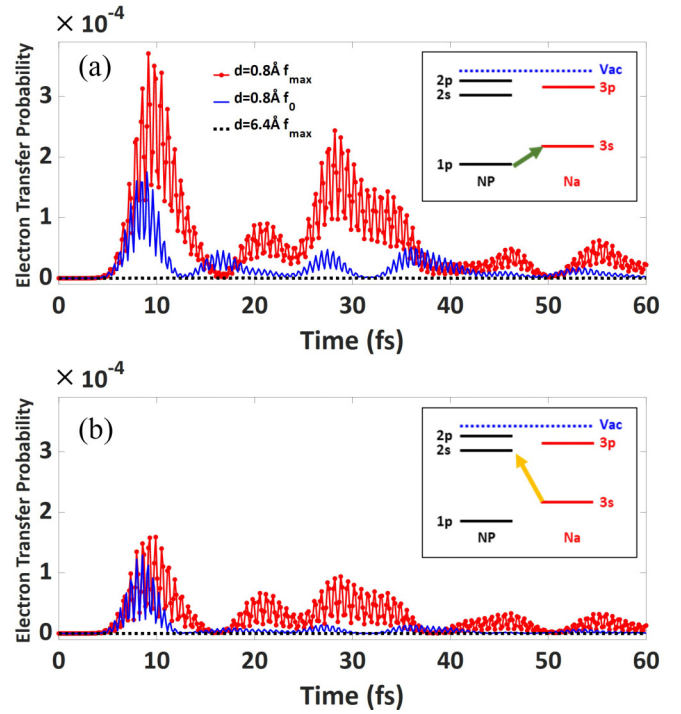


FIG. 4. Calculation of the time-dependent orbital projections, which represent the probability of electron transfer between the NP and Na. (a) Electron transfer from NP $1p$ to Na $3s$, and (b) electron transfer from Na $3s$ to NP $2s$. The black dashed, blue solid, and red dotted curves correspond to the three conditions ($f_0$, $d = 6.4$ Å), ($f_0$, $d = 0.8$ Å), and ($f_{max}$, $d = 0.8$ Å), respectively.

OH. The charge transfer channel slightly opens and a small number of hot charge carriers can undergo transfer between the NP and Na as they get close [39,40]. Meanwhile, their orbitals start to strongly hybridize by the electromagnetic interactions. These effects result in a redistribution of electron density and energy levels, which severely disrupts the isolated plasmonic resonance modes of the NP, leading to a sharp decrease in emitted current. Nevertheless, the maximum emission current still originates from NFE, with $f_{max}$ only experiencing a slight frequency shift from $f_0$. Therefore, both $I_{max}$ and $I_0$ exhibit a noticeable decrease in this case.

When $d < 1.6$ Å, it is noteworthy that $I_{max}$ exhibits a sharp increase to more than 2.07 times compared to $I_0$, while $f_{max}$ is deviated significantly from $f_0$ in Fig. 3(b). This significant enhancement in $I_{max}$ is attributed to the decrease and eventually vanishing of the potential barrier between the NP and Na, which leads to the opening for the collective transfer of electrons, known as the generation of the CTP, and subsequently enhances the emission process. Due to the frequency of the CTP being much lower than the original plasmonic resonance frequency of the NP, $f_{max}$ also undergoes a significant reduction. On the contrary, the presence of the charge transfer significantly disturbs the original plasmonic resonant mode of the NP and the emission of the emitter at $f_0$, resulting in a significant difference in emission current, as shown by the blue curve in Fig. 3(a).

According to the above analysis, it is easy to understand the peak of $I_{max}$ and $I_0$ around $d = 4$ Å under the simultaneous influence of OH and NFE. As $d$ decreases from 9.6 to 4 Å, the NFE plays a dominant role in enhancing the photoemission current. The smaller $d$ leads to stronger field enhancement and larger emission current of Na, which is revealed by the charge density around Na in Figs. 10(a)–10(c) in Appendix C. However, in the range $2.4 < d < 4$ Å, OH significantly affects the plasmonic mode of the NP illustrated by the charge density in Figs. 10(c)–10(e) and thus the weakened NFE reduces the induced charge density of Na and the emission current. As a result, the gradual interchange of dominant mode between OH and NFE results in a local maximum value around $d = 4$ Å. Further deceasing $d$ ($d < 2.4$ Å), the barrier between the NP and Na vanishes and electrons are able to transfer collectively, allowing the existence of the CTP and making an increase of emission current.

### C. Electron transfer probability

In order to further investigate the interactions between the NP and Na, we calculated the electron transfer probability between orbitals under three conditions, ($f_{max}$, $d = 0.8$ Å), ($f_0$, $d = 0.8$ Å), and ($f_0$, $d = 6.4$ Å), with their corresponding photoemission annotated by arrows labeled 1, 2, and 3 in Fig. 3. In Figs. 4(a) and 4(b), under the condition ($f_{max}$, $d = 0.8$ Å), a strong probability of electron transfer between the NP and Na is evident, represented by the red dotted curve.
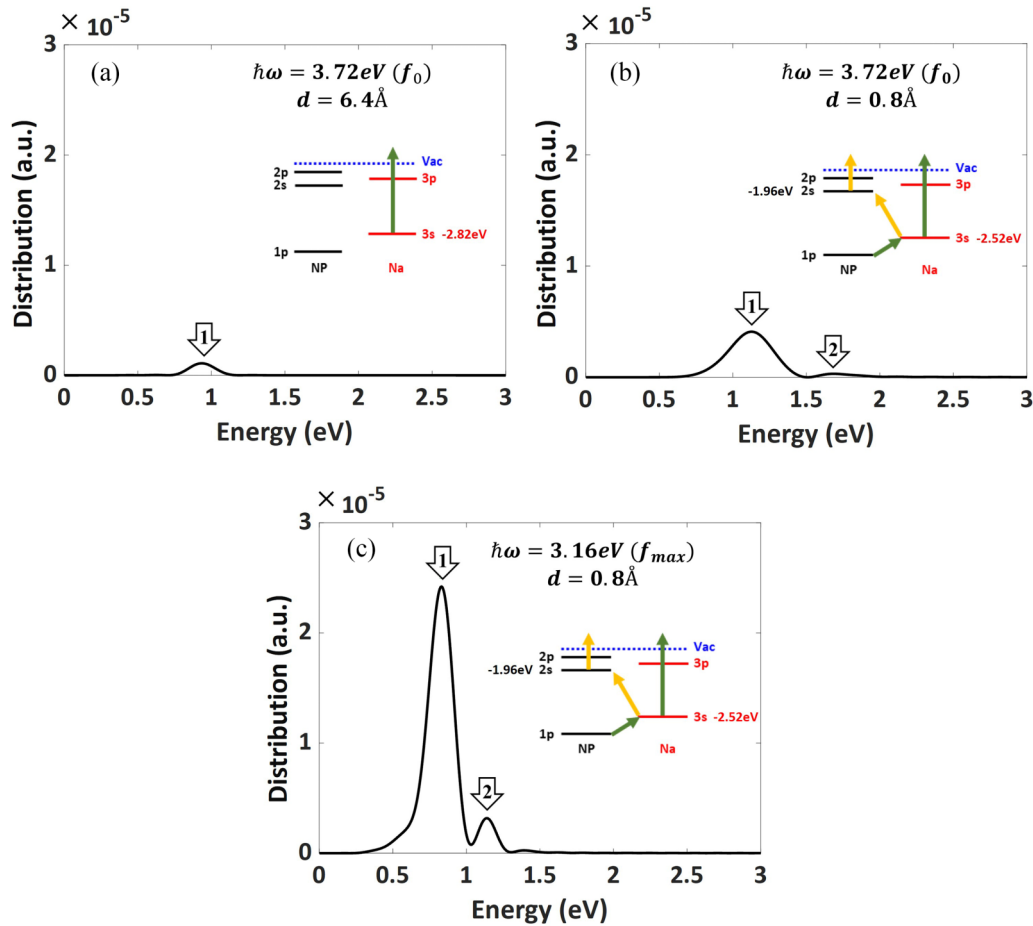
FIG. 5. Calculated energy spectrum of photoemission electrons under three conditions. Incident photon energy and distance between NP and Na: (a) $\hbar\omega = 3.72$ eV and $d = 6.4$ Å, (b) $\hbar\omega = 3.72$ eV and $d = 0.8$ Å, and (c) $\hbar\omega = 3.16$ eV and $d = 0.8$ Å. Insets are the schematic of electron transfer and emission path.

When the distance $d$ remains small but the laser frequency is changed to $f_0$, there is still a probability of electron transfer, as illustrated by blue solid curve, although the intensity is reduced compared to that of $f_{max}$. On the other hand, with a relatively large distance ($d = 6.4$ Å), the black dashed curve shows that the probability of electron transfer from Na to the NP decreases to nearly zero. This indicates that, under the large-distance condition, electrons in Na are difficult to transfer to the NP; therefore, CTPs have little assistance in the process of photoemission in this situation.

Figure 4(a) shows the probability of electron transfer from the NP-HOMO (NP $1p$) to the Na-HOMO (Na $3s$). The strong transfer probability indicates that a significant number of electrons transfer from the NP-HOMO to the Na-HOMO for the condition ($f_{max}$, $d = 0.8$ Å). Because electrons are mainly emitted from the Na-HOMO, this process can supplement the photoemission of ground-state electrons in Na, effectively enhancing the emission current. Figure 4(b) shows the probability of electron transfer from the Na-HOMO (Na $3s$) to the NP-LUMO (NP $2s$). The similar but lower transfer probability indicates that a certain number of electrons also transfers from the Na-HOMO to the NP-LUMO for the condition ($f_{max}$, $d = 0.8$ Å). The overall periodic variation in the curve is attributed to the presence of a pulse envelope in the incident femtosecond laser. The sharp peaks represent the oscillation of the CTP. Due to the relatively coarse time sampling and the modulus calculations, the periodic oscillation results appear entirely as positive values.

### D. Analysis of emission pathways from the energy spectrum

By examining the energy distribution of photoemission electrons from Na-HOMO (Na $3s$), further insights can be gained into the emission process under the above-mentioned three different conditions. The electron energy spectrum of the plasmonic emitter is calculated by the sampling point methods [35]. During the photoemission process, electrons within the orbitals absorb a fixed photon energy and overcome the surface barrier to emit. As a result, the energy of the emitted electrons is equal to the incident photon energy ($\hbar\omega$) minus the energy of the orbital.

By calculating the energy spectrum of the emitted electrons, we can examine the distribution and characteristics of the emitting pathways, which is valuable for understanding the photoemission process and the energy transfer dynamics within the plasmonic emitter.

As shown in Fig. 5, the calculation results of the energy distribution of emission electrons further reveal their pathways.

It can be observed that, in all three cases, there is a prominent peak in the energy distribution. This peak corresponds well to the energy difference between the incident laser and the Na-HOMO (Na $3s$) [Fig. 5(a), $3.72 - 2.82 = 0.9$ eV; Fig. 5(b), $3.72 - 2.52 = 1.2$ eV, and Fig. 5(c), $3.16 - 2.52 = 0.64$ eV, represented by the arrows labeled 1 in the figure), as the electron escaping from the material after absorbing a photon in the Na-HOMO. Comparing the magnitudes of the green peaks, it is evident that the peak significantly increases at $d = 0.8$ Å, which indicates that the transfer process from the NP-HOMO to the Na-HOMO effectively supplements the missing electrons and thereby enhances the emission current.

When the distance $d$ is 6.4 Å, as shown in Fig. 5(a), the energy distribution curve exhibits only a single peak and the emitting electrons are primarily generated from the Na-HOMO directly without undergoing any electron transfer. As a result, the electron energy distribution is more concentrated in this case, but the emitting current is relatively low.

In contrast, Figs. 5(b) and 5(c) demonstrate that when $d = 0.8$ Å, the electron energy distribution reveals a distinct side peak with lower intensity and higher energy marked by the arrows labeled 2. The side peak results from the emitted electrons from the NP-LUMO (NP $2s$) [Fig. 5(b), $3.72 - 1.96 = 1.76$ eV; Fig. 5(c), $3.16 - 1.96 = 1.2$ eV, represented by the arrows labeled 2 in the figure]. In Figs. 5(b) and 5(c), the calculated spectra exhibit similar peak shapes, with only differences in peak magnitudes. This indicates that electrons undergo CTP enhanced emission processes in such proximity, but the CTP enhancement at $f_{max}$ is stronger than that at $f_0$.

Therefore, since the overlap of electron orbitals of the NP and Na in real space leads to a high probability of collective electron transfer between them as a CTP, the energy distribution reveals two pathways for enhancing photoemission electrons in close proximity. First, a significant transfer of electrons from the NP-HOMO to the Na-HOMO effectively replenishes the missing electrons in the Na-LUMO. The CTP between them allows a large number of electrons to transfer between Na and the NP, thus effectively enhancing the photoemission current. Second, by absorbing the incident photons, electrons in the Na-HOMO significantly transfer to the NP-LUMO and emit as free electrons, thus establishing a new emission pathway.

## IV. CONCLUSIONS

In conclusion, the photoemission of a plasmonic emitter consisting of a NP and Na is investigated theoretically and numerically by using real-time TDDFT. It is revealed that the optimal laser excitation frequency for the electron emitter gradually deviates away from the classical plasmonic resonance frequency of the NP with the decrease in distance $d$, which contradicts the classical theory. And the optical laser frequency leads to a 2.07-fold increase in the maximum emission current compared to the original plasmonic resonant frequency of the NP. This is because the CTP instead of the NFE plays a crucial role in improving the photoemission current at a very close distance. The underlying mechanisms for this increased emission are uncovered by studying the orbital projections and energy distribution calculation. It is found

that a significant transfer of electrons from the NP-HOMO to the Na-HOMO effectively replenishes the missing electrons in the Na orbital. Also, electrons in the Na-HOMO absorb incident photons, significantly transfer to the NP-LUMO, and emit as free electrons, thus establishing a new emission pathway.

This work provides insights into the plasmon-enhanced photoemission process in NP-Na emitter systems, highlighting the importance of the CTP and shedding light on the underlying mechanisms. Despite the smaller scale of the plasmonic emitter model in this study, the results enable us to predict plasmonic responses in practical applications dependent on distance and frequency. By controlling the interaction mechanisms between the plasmon and emitter, significant electron emission with less reliance on laser parameters can be achieved. This knowledge can be valuable for future development of plasmon-enhanced photoemission electron sources.

## APPENDIX A: COMPUTATIONAL METHODS

We perform TDDFT using the OCTOPUS code [41]. The exchange-correlation functional is described by LDA and electron-ion interaction is represented by Troullier-Martins pseudopotentials. We use a jellium sphere model to describe the plasmonic NP. The Wigner-Seitz radius of Au species, $r_s$,
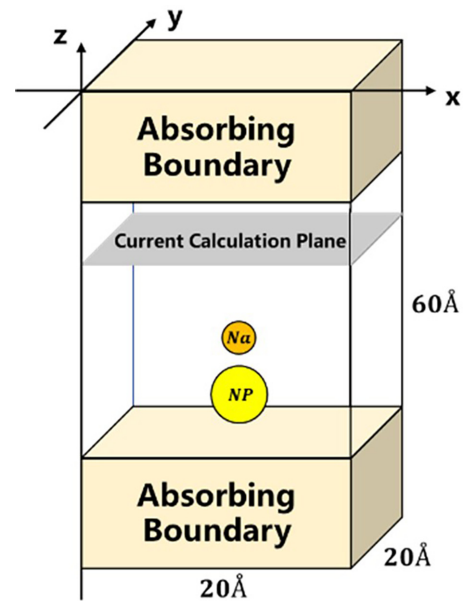


FIG. 6. Simulation box is a parallel pipe with absorption boundaries at the end of the $z$ axis. Na is placed at the origin and the NP is placed near Na, forming a plasmonic nanoparticle-metal emitter. The current calculation plane is set perpendicular to the $z$ axis at 20 Å across the simulation region.
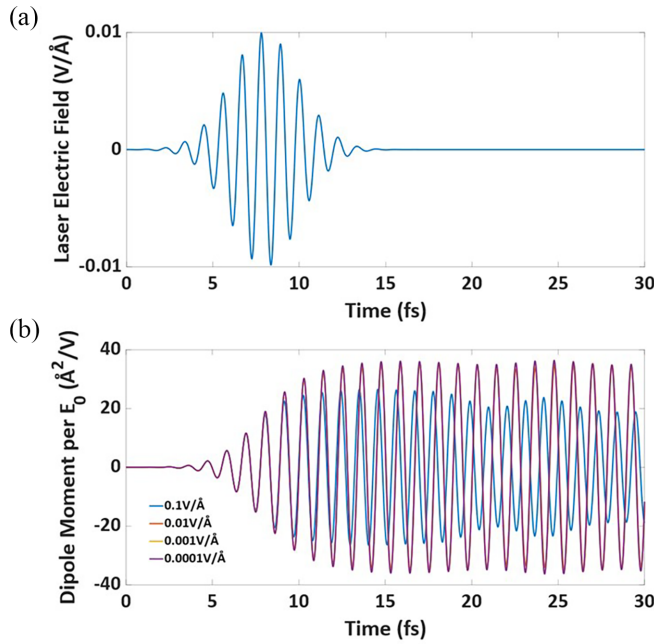
(a)



(b)



FIG. 7. (a) The electric field of the incident Gaussian-shaped laser pulse. (b) Dipole moment of the NP under different incident laser intensity at the NP resonant frequency. The curve at 0.1 V/Å exhibits significant changes compared to those of other conditions, while the curves at 0.01, 0.001, and 0.0001 V/Å almost coincide.

is 1.6 Å and the total electron number in jellium is 8. The shape of the simulation box is a parallel pipe with absorption boundaries at the end of both sides of the $z$ axis, as shown in Fig. 6. Lengths of the box are 20, 20, and 60 Å along the $x$, $y$, and $z$ axes, respectively. The absorption boundaries are set to prevent reflections of electrons. The Na atom is placed at the origin and the Au NP is placed near the Na separated by a distance $d$ along the $z$ axis, forming a plasmonic NP-metal junction emitter. The grid spacing is 0.4 Å, considering both the costs of calculation and accuracy of the results. The current calculation plane is set perpendicular to the $z$ axis at 20 Å across the simulation region. We calculate current flow



FIG. 9. Calculated electric potential with variance distance. At $d = 9.6$ Å, there is a significant potential barrier present at $z = -5$ Å; however, at $d = 0.8$ Å, the barrier between Na and the NP almost disappears.

transverse through the plane in every 50 iterations and add up.

The Gaussian-shaped laser pulse,

$$\boldsymbol{E}(t) = F \cos(\omega t) \exp\left[-\frac{(t - t_0)^2}{2\tau^2}\right],$$

is introduced to excite the electrons as shown in Fig. 7(a), where the pulse width is $\tau = 2$ fs and maximum intensity is reached at time $t_0 = 8$ fs. Laser field is $z$-direction polarized. When needed, external static fields directly induce the emitter at the beginning of time propagation. Each calculation performs 20 000 steps with a time step of 0.003 fs. We calculate normalized dipole moments of the resonant NP under different incident laser intensity. From Fig. 7(b), the laser intensity is set as 0.01 V/Å ensuring the linear response regime of the excited dipole moment, as the following absorption spectra and charge density differences are calculated based on impulse responses.
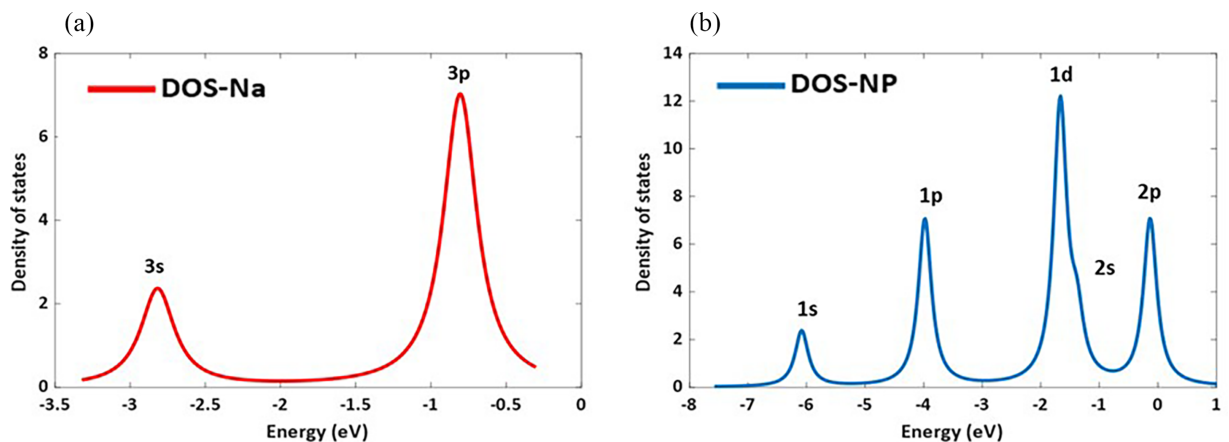
(a)



(b)



FIG. 8. (a) The density of states of Na clearly displays two orbitals, Na 3$s$ and Na 3$p$. (b) The density of states of the NP shows several electron orbitals, including NP 1$s$, NP 1$p$, NP 1$d$, NP 2$s$, and NP 2$p$.
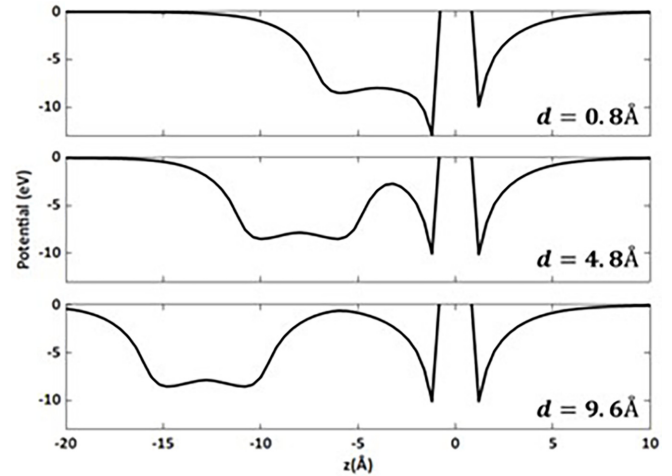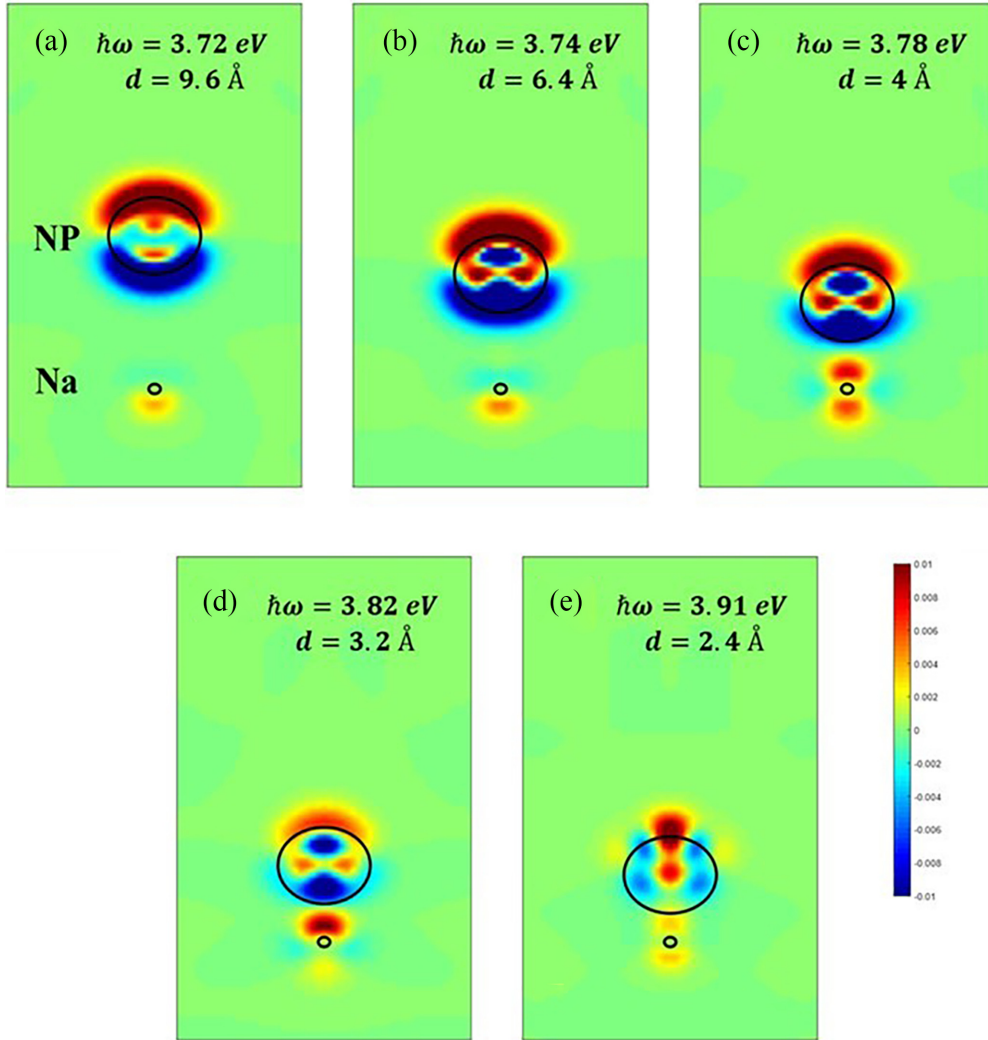
FIG. 10. Induced charge density of Na as a function of $d$: (a) $\hbar\omega = 3.72$ eV and $d = 9.6$ Å, (b) $\hbar\omega = 3.74$ eV and $d = 6.4$ Å, (c) $\hbar\omega = 3.78$ eV and $d = 4$ Å, (d) $\hbar\omega = 3.82$ eV and $d = 3.2$ Å, and (e) $\hbar\omega = 3.91$ eV and $d = 2.4$ Å. The NP and Na are excited by the optimal light frequency $f_{\max}$.

## APPENDIX B: DENSITY OF STATES AND ELECTRIC POTENTIAL

We calculate the DOS of Na and the NP, respectively, including all the extra unoccupied states under vacuum energy level. As our calculation results show in Figs. 8(a) and 8(b), the eigenvalues of Na occupied and unoccupied energy levels are $-2.818$ and $-0.805$ eV, related to the $3s$ and $3p$ orbitals. There are more orbitals in the NP including $1s$, $1p$, $1d$, $2s$, and $2p$. The highest occupied orbital energy is $-3.973$ eV, corresponding to the $1p$ orbital of the NP and the lower occupied energy level is the $2s$ orbital at $-6.087$ eV.

The charge transfer possibility can be briefly reflected by the calculated electric potential in Fig. 9. Na is placed at the origin while the NP approaches it from the negative $z$ axis. The potential barrier between Na and the NP lowers and even vanishes as the distance $d$ decreases. We find that the charge transfer channel opens completely when two particles are close enough, which ought to strongly enhance the photoemission current with more carrier transfers.

## APPENDIX C: CHARGE DENSITY DIFFERENCES

As shown in Fig. 10, there are intriguing finds in the charge density calculations. The calculation results of charge density demonstrate that the NFE becomes more pronounced as the distance $d$ decreases to 4 Å. In Figs. 10(a)–10(c), as $d > 4$ Å, a clear resonance mode is exhibited in the NP, leading to a quite large amount of induced charge density in the Na atom. As $2.4 < d < 4$ Å, OH significantly affects the plasmonic mode of the NP and the field around the NP is obvious weaker as illustrated by Figs. 10(d) and 10(e), which leads

to a drop of field enhancement of Na and photoemission current.

**APPENDIX D: PROJECTED DENSITY OF STATES**

In the investigation of complex systems, the PDOS emerges as a pivotal tool for analyzing the electronic behavior of distinct elements or atomic species. The PDOS allows for a detailed examination of how specific elements within multielement materials contribute to the overall electronic structure, enabling a deeper insight into the material's properties and behaviors.

Furthermore, the PDOS is instrumental in illustrating the distribution of various types of electronic states, such as $s$, $p$, and $d$ orbitals. By providing a detailed energy distribution of different electronic states, the PDOS facilitates a greater understanding of the material's electronic interactions and bonding characteristics, which are fundamental to predicting and explaining its physical properties [19,42].

Figure 11(a) shows the DOS of the NP-Na emitter, which is actually the lowest blue curve (corresponding to $d = 0.8$ Å) in Fig. 2(b). And Figs. 11(b)–11(d) display the PDOS calculation results at $d = 9.6$ Å (red dashed lines) and $d = 0.8$ Å (blue solid lines). From Fig. 11(b), it can be observed that, due to the reducing of $d$ (the overlapping of electron clouds), there is a significant splitting of the energy levels of the Na $3s$ orbital, and the higher energy peak is 2.52 eV at $d = 0.8$ Å. Figure 11(c) shows the slight changes in the NP $1p$ orbital when decreasing $d$, which indicates that the NP $1p$ orbital is not significantly affected due to the overlapping of electron clouds. Figure 11(d) displays that reducing $d$ (the overlapping of electron clouds) broadens the energy levels of the NP $2s$ orbital and shifts the peak to 1.96 eV at $d = 0.8$ Å. According to the peak value of the energy level in Figs. 11(b) and 11(d), the energy levels of Na $3s$ and NP $2s$ orbitals are simplified and marked as 2.52 and 1.96 eV, respectively, as depicted in the inset of Figs. 5(b) and 5(c).
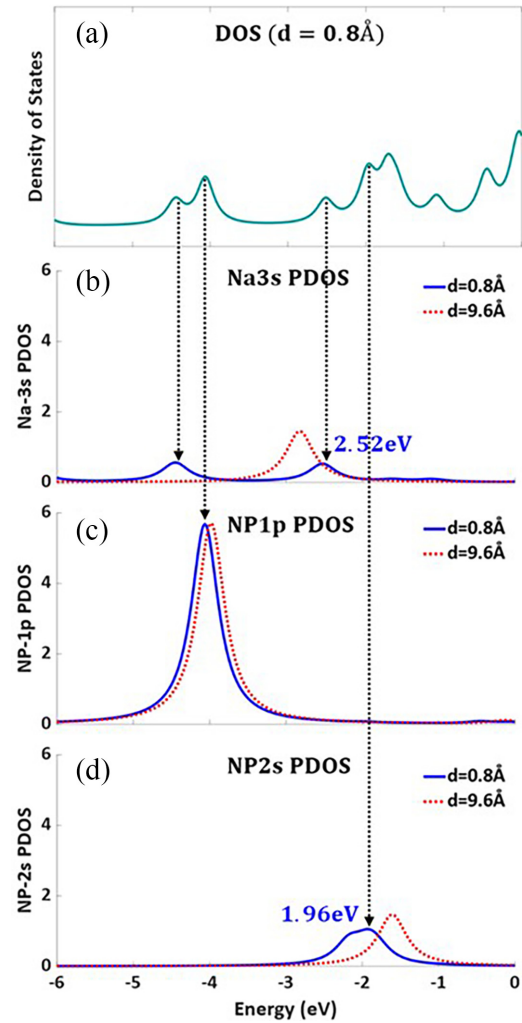


FIG. 11. (a) Density of states of NP-Na emitter as distance $d = 0.8$ Å. Projected density of states of (b) Na $3s$, (c) NP $1p$, and (d) NP $2s$ as distance $d = 9.6$ Å (marked by red dotted line) and $d = 0.8$ Å (marked by blue solid line), respectively.

[1] K. L. Kelly, E. Coronado, L. L. Zhao, and G. C. Schatz, The optical properties of metal nanoparticles: The influence of size, shape, and dielectric environment, J. Phys. Chem. B **107**, 668 (2003).

[2] A. W. Castleman Jr., and S. N. Khanna, Clusters, superatoms, and building blocks of new materials, J. Phys. Chem. C **113**, 2664 (2009).

[3] J. A. Schuller, E. S. Barnard, W. Cai, Y. C. Jun, J. S. White, and M. L. Brongersma, Plasmonics for extreme light concentration and manipulation, Nat. Mater. **9**, 193 (2010).

[4] D. E. Beck, Self-consistent calculation of the eigenfrequencies for the electronic excitations in small jellium spheres, Phys. Rev. B **35**, 7325 (1987).

[5] H. D. N. Brodusch and R. Gauvin, *Field Emission Scanning Electron Microscopy* (Springer, Berlin, 2018).

[6] A. Ul-Hamid, *A Beginners' Guide to Scanning Electron Microscopy* (Springer, Cham, 2018).

[7] D. C. Bell, Low voltage high-resolution transmission electron microscopy, in *Low Voltage Electron Microscopy: Principles and Applications* (John Wiley & Sons Inc., Hoboken, NJ, 2012), pp. 97–117.

[8] A. H. Zewail, Four-dimensional electron microscopy, Science **328**, 187 (2010).

[9] A. Polyakov, C. Senft, K. F. Thompson, J. Feng, S. Cabrini, P. J. Schuck, H. A. Padmore, S. J. Peppernick, and W. P. Hess, Plasmon-enhanced photocathode for high brightness and high repetition rate x-ray sources, Phys. Rev. Lett. **110**, 076802 (2013).

[10] R. K. Li, H. To, G. Andonian, J. Feng, A. Polyakov, C. M. Scoby, K. Thompson, W. Wan, H. A. Padmore, and P. Musumeci, Surface-plasmon resonance-enhanced multiphoton emission of high-brightness electron beams from a nanostructured copper cathode, Phys. Rev. Lett. **110**, 074801 (2013).

[11] A. Ono, N. Shiroshita, M. Kikawada, W. Inami, and Y. Kawata, Enhanced photoelectron emission from aluminum thin film by surface plasmon resonance under deep-ultraviolet excitation, J. Phys. D: Appl. Phys. **48**, 184005 (2015).

[12] D. B. Durham, F. Riminucci, F. Ciabattini, A. Mostacci, A. M. Minor, S. Cabrini, and D. Filippetto, Plasmonic lenses for tunable ultrafast electron emitters at the nanoscale, Phys. Rev. Appl. **12**, 054057 (2019).

[13] S. Keramati, A. Passian, V. Khullar, J. Beck, C. Uiterwaal, and H. Batelaan, Surface plasmon enhanced fast electron emission from metallised fibre optic nanotips, New J. Phys. **22**, 083069 (2020).

[14] J. A. Scholl, A. L. Koh, and J. A. Dionne, Quantum plasmon resonances of individual metallic nanoparticles, Nature (London) **483**, 421 (2012).

[15] A. Manjavacas and F. J. García de Abajo, Tunable plasmons in atomically thin gold nanodisks, Nat. Commun. **5**, 3548 (2014).

[16] M. Ludwig, G. Aguirregabiria, F. Ritzkowsky, T. Rybka, D. C. Marinica, J. Aizpurua, A. G. Borisov, A. Leitenstorfer, and D. Brida, Sub-femtosecond electron transport in a nanoscale gap, Nat. Phys. **16**, 341 (2019).

[17] X. Shao, A. Srinivasan, W. K. Ang, and A. Khursheed, A high-brightness large-diameter graphene coated point cathode field emission electron source, Nat. Commun. **9**, 1288 (2018).

[18] E. Selenius, S. Malola, and H. Häkkinen, Analysis of localized surface plasmon resonances in spherical jellium clusters and their assemblies, J. Phys. Chem. C **121**, 27036 (2017).

[19] J. Fojt, T. P. Rossi, M. Kuisma, and P. Erhart, Hot-carrier transfer across a nanoparticle–molecule junction: The importance of orbital hybridization and level alignment, Nano Lett. **22**, 8786 (2022).

[20] E. Selenius, S. Malola, M. Kuisma, and H. Häkkinen, Charge transfer plasmons in dimeric electron clusters, J. Phys. Chem. C **124**, 12645 (2020).

[21] J. Zuloaga, E. Prodan, and P. Nordlander, Quantum description of the plasmon resonances of a nanoparticle dimer, Nano Lett. **9**, 887 (2009).

[22] D. C. Marinica, A. K. Kazansky, P. Nordlander, J. Aizpurua, and A. G. Borisov, Quantum plasmonics: Nonlinear effects in the field enhancement of a plasmonic nanoparticle dimer, Nano Lett. **12**, 1333 (2012).

[23] A. Babaze, R. Esteban, A. G. Borisov, and J. Aizpurua, Electronic exciton–plasmon coupling in a nanocavity beyond the electromagnetic interaction picture, Nano Lett. **21**, 8466 (2021).

[24] R. Sinha-Roy, J. Hurst, G. Manfredi, and P.-A. Hervieux, Driving orbital magnetism in metallic nanoparticles through circularly polarized light: A real-time TDDFT study, ACS Photonics **7**, 2429 (2020).

[25] J. Yan, Z. Yuan, and S. Gao, End and central plasmon resonances in linear atomic chains, Phys. Rev. Lett. **98**, 216602 (2007).

[26] Y. Luo and P. Zhang, Ultrafast optical-field-induced photoelectron emission in a vacuum nanoscale gap: An exact analytical formulation, Appl. Phys. Lett. **119**, 194101 (2021).

[27] G. Z. Kiss, P. Foldi, and P. Dombi, Ultrafast plasmonic photoemission in the single-cycle and few-cycle regimes, Sci. Rep. **12**, 3932 (2022).

[28] Y. Luo and P. Zhang, Optical-field-induced electron emission in a dc-biased nanogap, Phys. Rev. Appl. **17**, 044008 (2022).

[29] P. Hohenberg and W. Kohn, Inhomogeneous electron gas, Phys. Rev. **136**, B864 (1964).

[30] M. A. L. Marques and E. K. U. Gross, Time-dependent density functional theory, Annu. Rev. Phys. Chem. **55**, 427 (2004).

[31] J.-L. Calais, Density-functional theory of atoms and molecules, Int. J. Quantum Chem. **47**, 101 (1993).

[32] C. Li, K. Chen, M. Guan, X. Wang, X. Zhou, F. Zhai, J. Dai, Z. Li, Z. Sun, S. Meng *et al.*, Extreme nonlinear strong-field photoemission from carbon nanotubes, Nat. Commun. **10**, 4891 (2019).

[33] U. De Giovannini, H. Hubener, and A. Rubio, A first-principles time-dependent density functional theory framework for spin and time-resolved angular-resolved photoelectron spectroscopy in periodic systems, J. Chem. Theory Comput. **13**, 265 (2017).

[34] U. De Giovannini, H. Hubener, S. A. Sato, and A. Rubio, Direct measurement of electron-phonon coupling with time-resolved ARPES, Phys. Rev. Lett. **125**, 136401 (2020).

[35] P. Wopperer, U. De Giovannini, and A. Rubio, Efficient and accurate modeling of electron photoemission in nanostructures with TDDFT, Eur. Phys. J. B **90**, 51 (2017).

[36] G. Aguirregabiria, D.-C. Marinica, M. Ludwig, D. Brida, A. Leitenstorfer, J. Aizpurua, and A. G. Borisov, Dynamics of electron-emission currents in plasmonic gaps induced by strong fields, Faraday Discuss. **214**, 147 (2019).

[37] K. Zhang and H. Zhang, Plasmon coupling in gold nanotube assemblies: Insight from a time-dependent density functional theory (TDDFT) calculation, J. Phys. Chem. C **118**, 635 (2014).

[38] T. Perera, S. D. Gunapala, M. I. Stockman, and M. Premaratne, Plasmonic properties of metallic nanoshells in the quantum limit: From single particle excitations to plasmons, J. Phys. Chem. C **124**, 27694 (2020).

[39] L. Román Castellanos, O. Hess, and J. Lischner, Single plasmon hot carrier generation in metallic nanoparticles, Commun. Phys. **2**, 47 (2019).

[40] A. S. Fedorov, P. O. Krasnov, M. A. Visotin, F. N. Tomilin, S. P. Polyutov, and H. Ågren, Charge-transfer plasmons with narrow conductive molecular bridges: A quantum-classical theory, J. Chem. Phys. **151**, 244125 (2019).

[41] N. Tancogne-Dejean, M. J. T. Oliveira, X. Andrade, H. Appel, C. H. Borca, G. Le Breton, F. Buchholz, A. Castro, S. Corni, A. A. Correa *et al.*, OCTOPUS, a computational framework for exploring light-driven phenomena and quantum dynamics in extended and finite systems, J. Chem. Phys. **152**, 124119 (2020).

[42] T. Rangel *et al.*, Can molecular projected density of states (PDOS) be systematically used in electronic conductance analysis? Beilstein J. Nanotechnol. **6**, 1247 (2015).